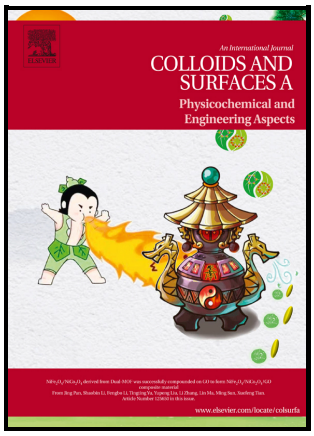

Construction and investigation on perovskite-type $SrTiO_3$ @ reduced graphene oxide hybrid nanocomposite for enhanced photocatalytic performance

G. Venkatesh, S. Vignesh, M. Srinivasan, G. Palanisamy, N. Elavarasan, K. Bhuvaneswari, P. Ramasamy, Manawwer Alam, Mohd Ubaidullah, Md Kausar Rasa

PII: S0927-7757(21)01392-3

DOI: https://doi.org/10.1016/j.colsurfa.2021.127523

Reference: COLSUA127523

To appear in: *Colloids and Surfaces A: Physicochemical and Engineering Aspects*

Received date: 22 July 2021
Revised date: 4 September 2021
Accepted date: 4 September 2021

Please cite this article as: G. Venkatesh, S. Vignesh, M. Srinivasan, G. Palanisamy, N. Elavarasan, K. Bhuvaneswari, P. Ramasamy, Manawwer Alam, Mohd Ubaidullah and Md Kausar Rasa, Construction and investigation on perovskite-type $SrTiO_3$ @ reduced graphene oxide hybrid nanocomposite for enhanced photocatalytic performance, *Colloids and Surfaces A: Physicochemical and Engineering Aspects,* (2021) doi:https://doi.org/10.1016/j.colsurfa.2021.127523

Construction and investigation on perovskite-type $SrTiO_3$ @ reduced graphene oxide hybrid nanocomposite for enhanced photocatalytic performance

G. Venkatesh [a]*, S. Vignesh [a], M. Srinivasan [a]*, G. Palanisamy [a], N. Elavarasan [a], K. Bhuvaneswari [b], P. Ramasamy [a], Manawwer Alam [c], Mohd Ubaidullah [c], Md Kausar Rasa [d]

[a] *SSN Research Centre, Sri Sivasubramaniya Nadar College of Engineering, Kalavakkam - 603 110, Tamil Nadu, India*

[b] *Department of Electronics and Communication Engineering, Sri Sivasubramaniya Nadar College of Engineering, Kalavakkam - 603 110, Tamil Nadu, India*

[c] *Department of Chemistry, College of Science, King Saud University, Riyadh - 11451, Saudi Arabia*

[d] *Department of Chemistry and Chemical Engineering, California Institute of Technology, 1200E, Pasadena CA - 91125, USA*

[*] ***Corresponding authors:*** *G. Venkatesh (venkeyphy@gmail.com); M. Srinivasan (srinivasanm@ssn.edu.in);*

Abstract

To construct rGO/$SrTiO_3$ nanocomposite using a facile hydrothermal synthetic approach for enhanced photocatalytic application. In this study, the structural, morphological, elemental, surface compositional, optical properties, and photocatalytic activity of rGO/$SrTiO_3$ nanocomposites were investigated. From the various analyses, the synthesized nanocomposites produce heterostructure formation between reduced graphene oxide (rGO) and $SrTiO_3$. By the optical analysis, the results showed that prepared ESG 10 photocatalyst has efficient charge separation and migration with suppressed recombination probability of photogenic charge carriers. The photocatalytic reactivity of the synthesised photocatalysts was evaluated by methylene blue (MB) aqueous dye and 2-nitrophenol (2-NP) degradation under UV-Visible (UV-Vis.) light irradiation. Therefore, the ESG 10 photocatalyst exhibited a maximum removal efficiency of 91 % and 81 % over MB dye and 2-NP, respectively. In contrast to other samples, the introduction of rGO could suggestively enhance the photocatalytic activity by increasing the amount of rGO, and the degradation rate was also reduced after the optimal level of rGO. The radicals involved in the degradation process are investigated by scavenger experiments. The recycle experiment reveals that the ESG 10

photocatalyst doesn't show any major loss of activity after 4 consecutive runs. Meanwhile, the possible reaction mechanism and interface characteristics are also discussed.

Keywords:

Nanocomposite; Photocatalysis; Reduced graphene oxide; Perovskite; Stability;

1. Introduction

The modernization of society, technology and industrialization cause various environmental issues. The various pollutant mixed into the groundwater resources affects the entire environment very badly [1,2]. The untreated effluents from plastics, cosmetics, food and textile industries directly discharged into the water system cause severe health issues to the humans [3,4]. Thus, various technologies have been followed to remove the effluents from wastewater. Amongst, photocatalysis constitutes the most hopeful option due to its efficiency, environment-friendly and promising remediation for the current environment deterioration [5,6]. Recently, perovskite materials with ABO_3 formula have gained attention owing to their attractive application in various technological fields [7].

Over the past decades, various semiconductor photocatalysts like TiO_2 [8,9], ZnO [10,11], $SrTiO_3$ [12] and g-C_3N_4 [13] etc [14–17] and perovskite alkaline earth titanates of $ATiO_3$ (A=Sr, Ca, Ba) have also been reported for effective hydrogen production by the photocatalytic process. Among various photocatalysts, $SrTiO_3$ has garnered attention with compelling properties in photocatalysis [18]. Moreover, $SrTiO_3$ has been one of the potentials and well-known semiconductor photocatalysts owing to its low cost, high chemical stability, biocompatibility and comparable optical property with the standard TiO_2 photocatalyst [19,20]. However, the reported investigations showed a wide band gap of $SrTiO_3$ which respond only in the ultraviolet (UV) solar spectrum and consequently showed its limitations in practical applications.

Recently, researchers have approached several methods to achieve and control the physical properties of $SrTiO_3$ with certain conditions to change the perovskite phase, morphology, particle size and crystal defects [21]. Various methods of synthesis have been reported such as sol-gel combustion [22], solvothermal [23], sol-gel hydrothermal [24] are available for synthesising $SrTiO_3$. However, these methods seek lower temperatures (180-260 °C) and a long-lasting heating time of about 18 to 48 h. Using these methods, the materials exhibit irregular formation in perovskite phases and poor optical property which is not optimized for desired applications [25]. So, the researchers have focused their attention on

the conventional method of a hydrothermal process for synthesising $SrTiO_3$ at a low-temperature level with a shorter time of heating [26]. This method is a time-efficient, cost-effective and facile type of approach. This approach is well suitable for designing $SrTiO_3$ with good optical property by controlling morphology with size and shape through purity and homogeneity form of chemicals [27].

Additionally, several researchers have intentionally modified to enhance the various properties of $SrTiO_3$ with metals, non-metals and combining carbon-based materials like rGO, gC_3N_4, graphene, etc [28–31]. The combination of these materials with $SrTiO_3$ could expand the band gap into the visible region and effectively reduces the crystallite size, which leads to enhance the photocatalytic activity [32–35]. Due to the high expensive of metals are not such a favourable option for designing an efficient photocatalyst. Moreover, Carbon-based material is a well and suitable option for enhancing photocatalytic efficiency.

Recently, graphene with high surface area, excellent hydrophobicity, higher stability, and electron acceptor properties has been utilized for the production of energy storage devices, sensors, organic compound absorption and separation etc [36]. Moreover, graphene with a 2D structure possesses higher electrical and thermal conductivity, electron mobility, chemical stability and mechanical strength [37,38]. The large surface area and good affinity of rGO possibly encourage the adsorption of organic molecules by π- π interactions (suitable for degrading pollutants). rGO acts as an acceptor and transporter of electrons, which enhances the photocatalytic activity of pollutant degradation and hydrogen evolution. This leads to more efficient charge separation and suppresses the recombination of electron-hole (e^-/h^+) pairs [39]. So, the researchers have turned up their attention towards carbon-based materials combined with $SrTiO_3$ materials. Based on previously reported articles, the combination of rGO/$SrTiO_3$ nanomaterials for the degradation of organic dyes was very rarely reported. For example, Tao Xian et al. [40] investigated $SrTiO_3$-graphene nanocomposites are utilized for the degradation of acid orange 7 by photocatalytic reduction method under UV light irradiation. A. Rosy and co-workers [35] evaluated the degradation performances of Rhodamine B (RhB) and Rose Bengal (RB) by rGO/$SrTiO_3$ heterostructured nanocomposite. Chenye He et al. [41] reported that $SrTiO_3$/graphene composite could generate an efficient pathway for degrading the RhB pollutant under UV light irradiation. Many reports have been reported with some drawbacks like long duration to degrade, higher band gap energy value, morphological defects, lesser photocatalytic efficiency. According to the previous discussions, the mixing, intercalation, doping or attachment of various materials enables us to take advantage of the many properties of each, therefore, the composites must

be specially crafted to incorporate advanced photocatalysts. To the best of our knowledge, the degradation of MB organic pollutant by rGO coupled $SrTiO_3$ nanocomposites *via* two-step facile hydrothermal method was not reported so far. So, we have decided to synthesis a low cost, environment-friendly, biocompatible nature and facile synthetic technique to achieve an effective attempt towards photocatalytic applications. Our main aim is to design the material with a composition of carbon materials with $SrTiO_3$ that may possess a tuned optimal band gap towards the UV or UV-Vis. light region, enhanced the charge separation and close surface interfacial interaction between these materials. Thus, the charge carriers can easily transfer and it tends to enhance the recombination of photogenerated e^-/h^+ pair.

In this work, the construction of different weight percentages (5, 10 & 20 Wt.%) of rGO-$SrTiO_3$ composites were prepared by facile hydrothermal method. $SrTiO_3$ nanoparticles (NPs) were decorated over reduced graphene oxide sheets that could be exploited to enhance photocatalytic efficiency. Various physicochemical properties of the prepared samples were evaluated by several characterization techniques. The evaluation of the photocatalytic dye degradation performance was confirmed using MB dye and 2-NP as a model pollutant under the UV-Vis. light exposure. Furthermore, the exposure of different radicals involved in the photocatalytic mechanism is also examined by scavenger experiments. The reusability and structural stability of the prepared samples were evaluated by recycling experiments. The possible charge transfer mechanism of the photo-degradation process *via* band alignment is also proposed.

2. Experimental section

2.1 Materials

All reagents were commercially purchased and directly used without any further purification. Titanium (IV) Isopropoxide (TTIP - 97%), Strontium chloride ($SrCl_2$ - 99.99%), Potassium Hydroxide (KOH - 97%), Ethyl alcohol (99.9%), Graphite powder (99.5%), Hydrogen peroxide (H_2O_2 - 30% purity), Sulfuric acid (H_2SO_4 - 97%), Hydrochloric acid (HCl - 38.0%), Potassium permanganate ($KMnO_4$ - 99.0%), Sodium nitrate ($NaNO_3$ - 99.0%), Methylene Blue (MB), 2-nitrophenol (2-NP), Benzoquinone (BQ - 98%), Ammonium oxalate (AO - 99%) and Isopropyl alcohol (IPA - 99.8%) were used as a precursor. De-ionized (DI) water was used for all the synthesis process.

2.2 Synthesis of graphene oxide/reduced graphene oxide

Graphene oxide (GO) was obtained using the ultrasonic modified Hummer's method [42]. 1 g of graphite and 6 g of $KMnO_4$ were added to 120 mL H_2SO_4 (98 %) and 13.3 mL H_3PO_4 (85 %). The mixture was then irradiated for 50 min in an ultrasonic bath at 30 °C to obtain a dark brown suspension. 1 mL H_2O_2 (30%) was gradually added to 266 mL of deionized (DI) water to reduce residual permanganate into soluble manganese ions. The colour of the mixture changed from dark brown to dark yellow. The mixture was filtered and washed with HCl aqueous solution to remove metal ions and then centrifuged at 6000 rpm. The filtered materials were washed with distilled water to remove residual acids and other impurities and the centrifugation step was repeated. Finally, the resulting solid was dried in an oven at 70 °C for 24 h to obtain GO.

2.3 Preparation of $SrTiO_3$ and rGO/$SrTiO_3$ nanocomposites

The preparation of $SrTiO_3$ is involved in co-solvent synthesis *via* facile hydrothermal route. 1.77 g of TTIP was dissolved in an appropriate amount of ethanol to form an initial precursor. 1.47 g of $SrCl_2$ and an appropriate amount of KOH were dissolved in 10 mL of DI water then added dropwise to the initial precursor under constant stirring for 30 mins. The obtained suspension was transferred to a hydrothermal autoclave and kept in an oven for 4 h at 200 °C. The resultant white precipitate was washed with acetic acid and DI water several times, then the washed products were dried in an airflow oven at 80 °C for 12 h. The yielded $SrTiO_3$ product was labelled as E SRT.

In the typical synthesis process, different weight percentage (5, 10 and 20 Wt. %) of graphene oxide was ultrasonicated by 30 mL DI water and 20 mL ethanol mixture solution for 2 h. After that, the dispersed solution was mixed with 20 mg of E SRT and stirred for 2 h to obtain a homogeneous suspension. Then, the mixture was transferred into a hydrothermal reactor and kept in a hot air oven with a maintaining temperature of 120 °C for 12 h. Notably, GO can be thoroughly reduced to rGO while the reaction temperature was maintained between 100 °C – 250 °C [43]. The resultant vessel was auto cooled at room temperature. Then the products were centrifuged, washed with DI water and ethanol for four times and further dried in a vacuum oven at 80 °C for 12 h. The schematic diagram of the synthesis procedure is shown in Fig. 1. Also, the synthesised resulting composite was labelled as ESG 5, ESG 10 and ESG 20.

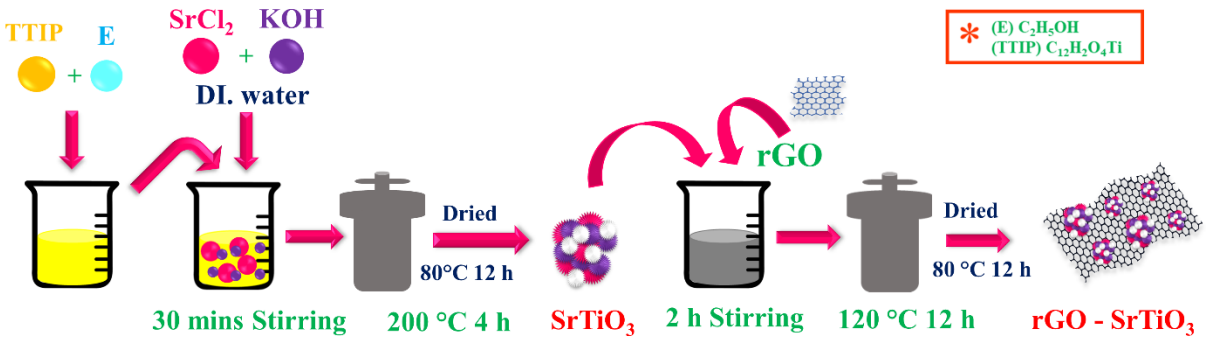

Fig. 1. Schematic representation of synthesis procedure for rGO/$SrTiO_3$ nanocomposite

2.3 Materials characterization

The synthesised products were analysed using X-ray diffraction (XRD) analysis (Rigaku D/Max Ultima III), Fourier transform infrared (FT-IR) spectra analytical tool (NEXUS 470 spectrometer) and UV-Visible absorption spectrophotometer (UV-Vis., JASCO V-770). The surface morphology and microstructure of the as-prepared samples were analyzed by using FESEM (Hitachi S-4800), HRTEM and EDX (JEOL JEM 2100) instrumental techniques. The chemical configuration and electronic structure of the samples were examined using X-ray photoelectron spectroscopy (XPS, ESCA 3400 spectrometer). The recombination process of the samples was accomplished by photoluminescence (PL) spectra (JASCO-spectrofluorometer FP-8200).

2.4 Photodegradation experiments

The performance of photocatalytic activity was evaluated by photodegradation of MB and the reduction of 2-NP in an aqueous medium under UV-Vis. irradiation with help of 500 W Halogen lamp as a light source. In a typical experiment, 10 mg of as-prepared photocatalysts were added in a 100 mg/L MB solution in the Pyrex double-layered beaker then stirred for several minutes. After the stirring process, the mixtures were placed in a dark room for 1 h to attain adsorption/desorption balance. Before initiating the degradation process the 0.1 mL of initial suspension was pipetted out. Then the Pyrex beaker was kept under illumination with a distance of 10 cm between the beaker and light source. During the experiment process, the beaker was circulated with water to prevent evaporation from the suspension. When the illumination starts, 0.1 mL of aliquots were taken out with 30 mins of time interval and immediately all the collected aliquots were centrifuged to evict the catalysts. The different dye concentration of the MB solution was measured using UV-Vis. absorption spectrophotometer. Furthermore, the same procedure was followed for all the

typical experiments with similar conditions for evaluating scavenger test, recycle and stability test. The degradation efficiency (%) of the synthesised photocatalysts were calculated by a typical empirical equation [44,45].

3. Results and discussion

3.1 XRD analysis

X-ray diffraction analysis was carried out to find the crystallographic structure and phase purity of the synthesised samples. Fig. 2, shows the XRD pattern of pure and other synthesised nanocomposites. The indexed diffraction peaks of E SRT observed at an angle 2θ = 22.5, 32.1, 39.6, 46.1, 57.3 and 67.2°, which are assigned to (100), (110), (111), (200), (211) and (220) planes, respectively. All the peaks were well consistent with the perovskite-type cubic phase structure identified by (JCPDS No. 40-1500). Furthermore, the synthesised nanocomposites also showed similar diffraction peaks of the E SRT sample. From Fig. 2 (a), A single peak of GO was observed at 11.04°. The introduction of rGO with different weight percentages shows no obvious changes in the corresponding XRD patterns. However, the tiny amount of rGO suggests no characteristic peaks were detected in the corresponding diffraction pattern and the influence of rGO loaded E SRT with different weight percentages shows variation in intensity suggests that the crystallinity and crystalline size were decreased [46]. The average crystalline size was calculated by Scherrer's equation, and the values are 36.4, 35, 33.1 and 34.9 nm for E SRT, ESG 5, ESG 10 and ESG 20 respectively. Comparatively smaller crystalline size implies a superior platform to transfer the charge carriers which is a necessary property of an efficient photocatalyst. The mechanism behind the inhibition of crystalline growth due to the inclusion of rGO has been presented elsewhere [47].

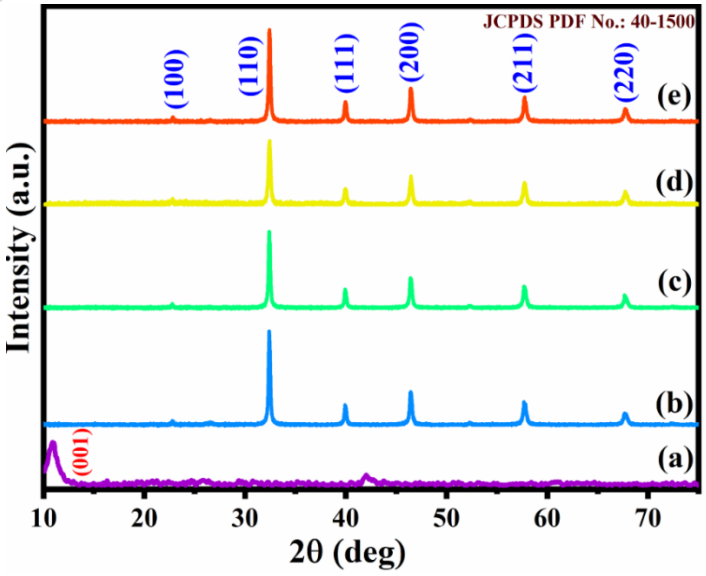

Fig. 2. XRD patterns for (a) GO, (b) E SRT, (c) ESG 5, (d) ESG 10 and (e) ESG 20 nanocomposite

3.2 Fourier transform infrared analysis

The functional group of the samples were identified by FT-IR analysis. The FT-IR spectra of the prepared samples are shown in Fig. 3. For the $SrTiO_3$ particles, the prominent absorption band at 570 cm^{-1} was in the region of stretching vibration of Ti-O-Ti [48]. The occurrence of the Ti-O bond and Sr-O bond were located by a combination of vibrations between the broadband at 500 cm^{-1} and 800 cm^{-1} [49]. The weaker peak at 1431 cm^{-1} was ascribed to C-H bending vibration. The presence of rGO absorption peaks at around 1217 cm^{-1} due to C=C asymmetric stretching vibration [50]. The band at 1626 cm^{-1} was assigned to the bending vibration of H-O-H from the surface absorbed H_2O, which revealed several peaks in the 1450-1700 cm^{-1} range. The peaks at 1550, 1626, and 1703 cm^{-1} could be attributed to the vibrations of carbamate esters, the C-C stretching of sp^2-hybridized carbon, and the C-O vibration of carboxylic groups, respectively [51,52]. The composition of rGO and $SrTiO_3$ was attributed to the interaction of C-H groups which might be formed by successful reduction of GO to rGO. The characteristic peak of Ti-O-Ti was observed in ESG 10 spectra proving the successful synthesis of rGO/$SrTiO_3$ nanomaterials.

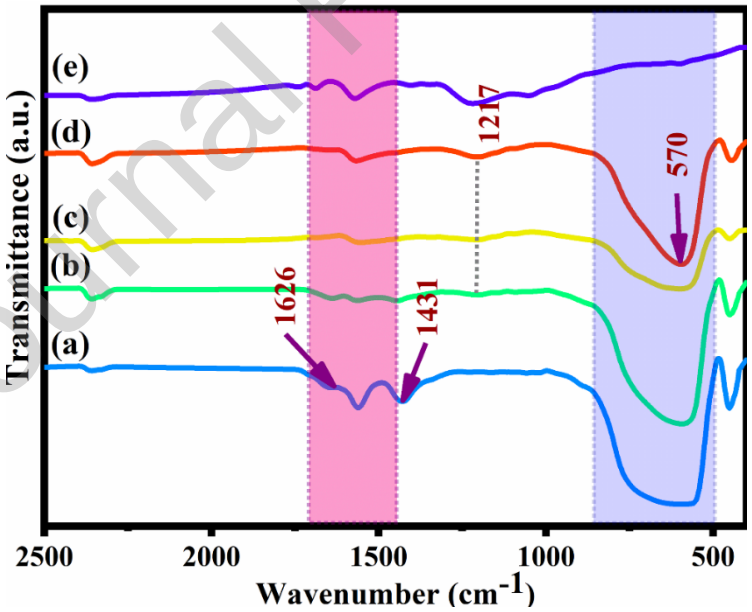

Fig. 3. FT-IR spectra for (a) E SRT, (b) ESG 5, (c) ESG 10, (d) ESG 20 nanocomposite and (e) GO

3.3 Morphological analysis

The determination of surface morphologies and microstructure was carried out by FESEM analysis. The surface morphology of the synthesised bare E SRT and ESG 10

nanocomposites were visualized in Fig. 4 (a-d). As shown in Fig. 4 (a & b), the synthesised pure E SRT particles have spherical like morphology with tiny particles on the surface. The unsmooth surface obtained due to the usage of solvent with low viscosity medium leads to agglomeration of nanoparticles. Moreover, low viscosity solvent has an ability with a high diffusion rate which enables a faster growth rate of nanostructures [53,54]. From Fig. 4 (c & d), the E SRT NPs have surrounded by the rGO sheets and in Fig. 4 (d), It is clearly seen that E SRT NPs were embedded on rGO sheets with strong interaction with graphene [55]. which can efficiently facilitate the interface charge separation and hamper carrier recombination. Therefore, it indicates that the successful formation of rGO with E SRT nanocomposite and the rGO led to good dispersion of E SRT on its surface.

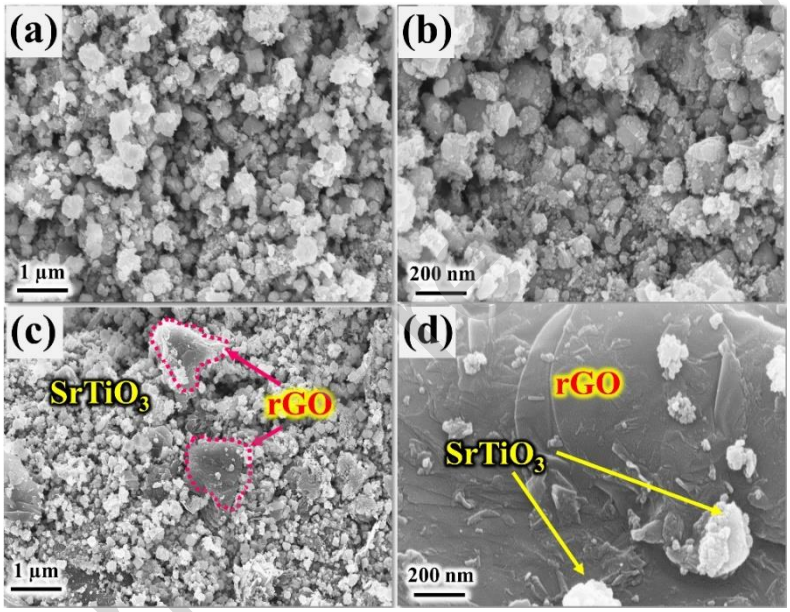

Fig. 4. FESEM images of (a, b) E SRT and (c, d) ESG 10 nanocomposite

3.4 HRTEM and EDX analysis

The crystalline nature and internal morphology of the prepared ESG 10 nanocomposite was visualized by HRTEM analysis as shown in Fig. 5 (a-e). From Fig. 5 (a & b), the E SRT spherical like agglomerated particles were spread over the surface of rGO sheets. It reveals that the E SRT sample was successfully wrapped over a 2-D layer of graphene sheets with no other impurities. The strongly influenced interaction between the combined heterostructure network of E SRT/rGO facilitates an exemplary charge transfer process which led to improving the catalytic activity. The clear interplanar lattice spacing was measured as 0.27 nm which clearly illustrates the atomic plane (110) of the E SRT sample as shown in Fig. 5 (e). The crystalline nature of the synthesized sample was obtained from the

SAED pattern shown in the inset of Fig. 5 (e). From these results, the synthesized ESG 10 nanocomposite provides advantageous properties for enhancing photocatalytic activity.

The presence of elements was confirmed by EDX analysis. From Fig. 5 (f) the EDX spectra confirm the successful formation of nanocomposite and the elements Sr, Ti, C and O were present in the ESG 10 nanocomposite. Also, no other impurity peaks were present in this composite. Further, the mass percentage of these elements were depicted in the inset Fig. 5 (e). Moreover, the element Cu arose from the copper grid used for HRTEM analysis.

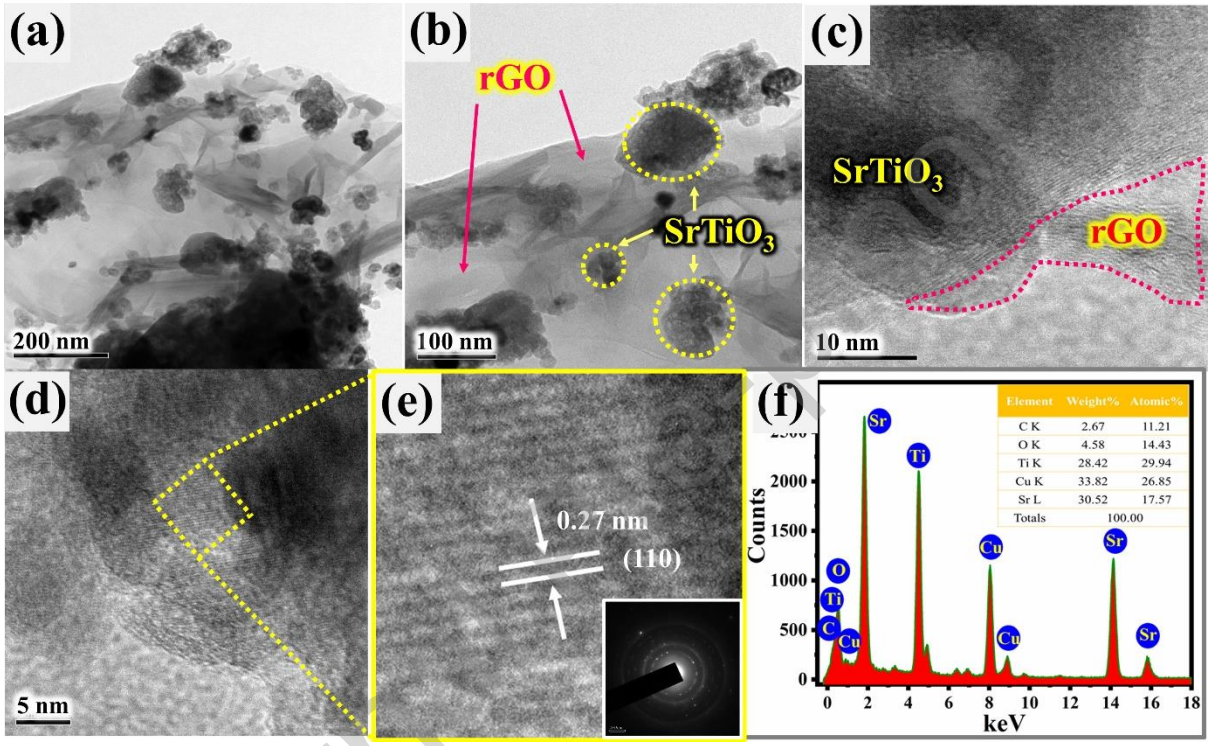

Fig. 5. (a – e) HRTEM images and (f) EDX spectra of ESG 10 nanocomposite

3.5 XPS analysis

The surface chemical configuration and electronic structure of the prepared rGO and ESG 10 photocatalysts were investigated by high-resolution XPS spectroscopic technique. The full range survey spectra of rGO and ESG 10 samples was demonstrated in Fig. 6 (a). As shown in Fig. 6 (b), the Sr 3d peaks with binding energy positions at 131.8 eV and 133.5 eV for ESG 10 sample is observed with two deconvoluted spectra, which are attributed to Sr $3d_{5/2}$ and Sr $3d_{3/2}$ states, respectively. From Fig. 6 (c), the binding energies indexed at 457.1 eV and 463 eV in the case of ESG 10 are ascribed to the states of Ti $2p_{3/2}$ and Ti $2p_{1/2}$ respectively [56]. In the perovskite structure of $SrTiO_3$, the binding energy values are corresponding to Ti with the oxidation state of 4^+ [57]. Fig. 6 (d) shows that the O 1s spectra of rGO was deconvoluted into two peaks with a binding energy value of 532.1 eV and 532.8 corresponds to the formation of C=O and C-O-C, respectively. Furthermore, in the case of

ESG 10 with two splitted peaks at 528.4 eV and 531.2 eV are ascribed to lattice oxygen (O_L), also the value of 531.2 eV due to surface hydroxyl groups (O_{OH}) respectively. The C 1s high-resolution spectra for the prepared samples are shown in Fig. 6 (e). For rGO, the C 1s spectra were deconvoluted into two peaks with the binding energy positions 284.6 and 288.9 are assigned to C=C, O-C=O, respectively and the deconvoluted two peaks appeared at ESG 10 with binding energy values of 283.6 eV and 287.6 eV ascribed to the formation of the Ti-C bond [58]. Notably, both the O 1s and C 1s peaks slightly shifted to lower binding energies due to O atoms are replaced by low energy electronegative C atoms, increasing the electron density around Sr and Ti atoms, respectively [59]. Furthermore, the occurrence of peak shifts in ESG 10 spectra towards lower binding energies attributed to strong interface bond between rGO and E SRT [60].

For photocatalysts, the overlap of the Ti atom's 3d orbit and the C atom's sp^2 orbit were facilitated a continuous pathway for electrons which enhancing the quick transportation of charge carriers. Additionally, it migrates that the charge recombination process which is the important factor for enhancing the photocatalytic activity. In comparison, this result suggests that the peaks in Fig. 6 (a-e), with no other functional groups were observed, hence it confirms that the effective formation of the high purity of the prepared samples.

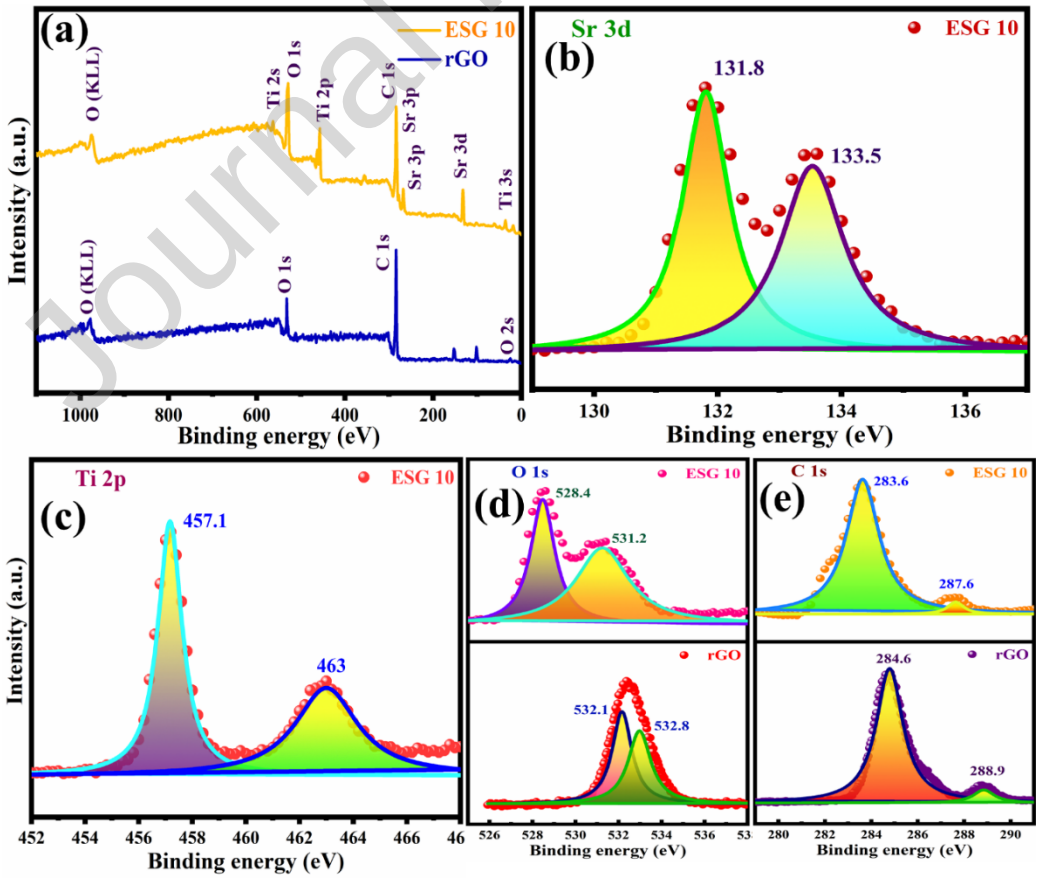

Fig. 6. XPS spectra (a) survey spectrum of rGO and ESG 10 nanocomposite, (b) Sr 3d, (c) Ti 2p spectrum of ESG 10 sample, (d) O 1s and (e) C 1s for rGO and ESG 10 nanocomposite

3.6 UV-Vis. absorption spectroscopy

The investigation of optical properties of the bare E SRT and ESG 10 nanocomposite were studied by UV-Vis. analysis. As shown in Fig. 7, the absorption edge of E SRT is exhibited at ~381 nm and ESG nanocomposites are exhibited from 387 to 400 nm. The absorption edge of the nanocomposites were red-shifted due to the addition of rGO. Thus, the nanocomposite attributes to interfacial formation between rGO/$SrTiO_3$. The shifts in absorption edge occurred due to the electronic transition from the O (p) state to Ti (d) state [61]. The absorption peak shifting indicates that the optical properties of $SrTiO_3$ NPs are varied by the implementation of rGO in $SrTiO_3$. The direct band gap values of the synthesized samples were calculated by Tauc relation as presented in equation (1) [61,62],

$$(\alpha h\nu)^2 = k\,(h\nu - E_g) \qquad (1)$$

Whereas, α - absorption coefficient, E_g - band gap energy of semiconductor, K - constant, hν - energy of a photon. From the above equation, the direct band gap of E SRT exhibited with 3.25 eV with an absorption edge at 381 nm, whereas the band gap (absorption edge) of the composites are gradually decreased from 3.20 eV (387 nm), 3.16 eV (392 nm) and 3.10 eV (400 nm) for ESG 5, ESG 20 and ESG 10, respectively. Furthermore, the ESG 20 photocatalyst shows a higher band gap which is due to the highest amount of graphene leads to hinders the light absorption property by E SRT NPs [63]. The excess content of rGO in the sample is considered to act as a recombination centre for photoinduced e^-/h^+ pairs [64]. Based on these results, the synthesised photocatalyst shows the variations in band gap energy values evidenced that the incorporation of different wt. % of rGO have modified the surface of crystal lattice could extend/affects the light absorption property which leads to enhance or deteriorates the photocatalytic degradation efficiency.

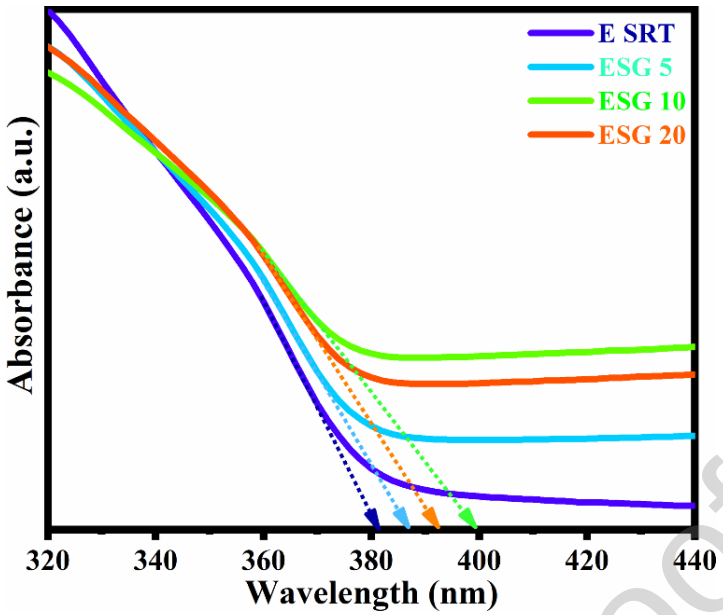

Fig. 7. UV-Vis. absorption spectra for E SRT, ESG 5, ESG 10 and ESG 20 nanocomposite

3.7 Photoluminescence analysis

The recombination behaviour of photo-excited charge carriers of E SRT and ESG 10 photocatalysts were evaluated by PL analysis. As shown in Fig. 8, the PL spectra were recorded in the range from 400 nm to 600 nm with 325 nm as an excitation wavelength. In general, A high recombination rate of photoexcited e^-/h^+ pairs is associated with a strong PL emission intensity, while a low recombination rate is associated with a weak PL emission intensity [65,66]. Hence, the synthesized ESG 10 photocatalyst shows weaker emission in PL intensity indicates a low recombination rate of photogenerated e^-/h^+ pairs compared to E SRT photocatalyst. Evidently from Fig. 8, the lower level of PL intensity effectively suppresses the recombination process due to electrons are quickly transferred from rGO to $SrTiO_3$ could enhance the photocatalytic activity. Furthermore, the amount of rGO increased above to its optimal value the agglomeration has occurred and it acts as a charge recombination centre that might enhance the PL intensity.

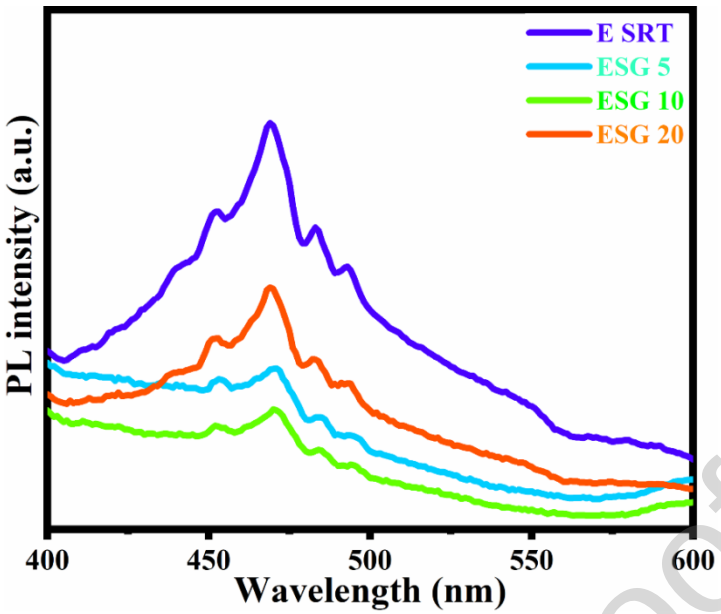

Fig. 8. Photoluminescence spectra of (a) E SRT, (b) ESG 5, (c) ESG 10 and (d) ESG 20 nanocomposites

3.8 Photocatalytic Activity

The photocatalytic capability of the synthesised E SRT and ESG 10 nanocomposites were examined by decomposition of MB dye with help of UV-Vis. light irradiation. The photodegradation performance of synthesized photocatalysts was obtained from UV-Vis. absorption spectra as shown in Fig. 9 (a & b). All the photocatalytic experiments are performed for 150 min of duration until the pollutant almost get to degrade. The degradation of MB dye was remains stable under light illumination as well as in the dark condition without photocatalyst. From Fig. 9 (d), the degradation efficiency chart of photocatalysts have been found to be 61, 83, 91 and 75 % for E SRT, ESG 5, ESG 10, ESG 20 samples respectively. Among all the synthesized photocatalysts ESG 10 shows enhanced photoactivity with 91 % of degradation efficiency in 150 min under UV-Vis. light exposure is shown in Fig. 9 (b). The ESG 10 photocatalyst showed favourable dye degradation performance than bare E SRT, which means the introduction of graphene played an important role as an obtained catalyst. The absence of O vacancies in the synthesized photocatalyst enables a lower recombination rate. Thus, the ESG 20 photocatalyst resultant in the lowest degradation efficiency. The kinetic pertaining plot (C_t/C_0) of different photocatalysts were mentioned in Fig. 9 (c), to indicate the comparison of photodegradation performance.

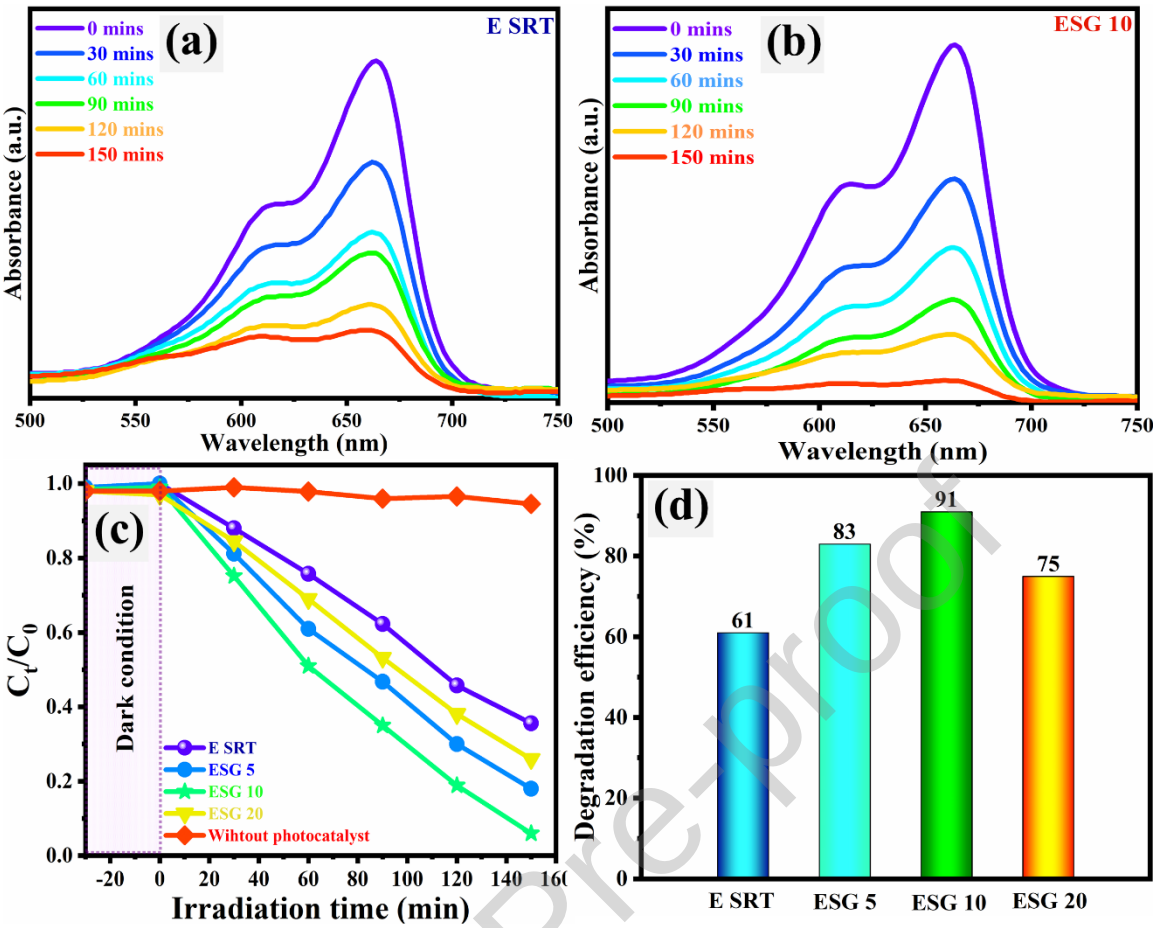

Fig. 9. (a) UV-Vis. absorption spectra of E SRT, (b) ESG 10, (c) photodegradation rate and (d) degradation efficiency chart for (E SRT, ESG 5, ESG 10, ESG 20) photocatalysts

To determine the linear relationship between irradiation time (t) *versus* slope of the plot of ln (C_0/C) for MB dye degradation over synthesized photocatalysts first-order kinetics plots were drawn and depicted in Fig. 10. From Fig. 10, the investigation was quantitatively found over MB degradation and the kinetics of degradation reaction processes are fitted to pseudo-first-order equation function model. The values are obtained using ln (C_0/C_t) = - kt whereas, k is apparently rate constant, C_0 is a preliminary concentration at 0 min, C_t is a concentration at t = t. All the photocatalytic degradation curves were consistently fit well with first-order kinetics (pseudo-order) for the synthesized photocatalysts. The highest degradation rate constant over MB dye degradation was observed for ESG 10 photocatalyst, which is about 2.5, 1.5 and 1.9 folds higher than that bare E SRT, ESG 5 & 20 nanocomposites respectively. The photodegraded reaction rate constant for the slope of a fitting line is determined from Fig. 10, and the values are 0.007, 0.0113, 0.0177 and 0.0089 min^{-1} for E SRT, ESG 5, ESG 10 and ESG 20 respectively.

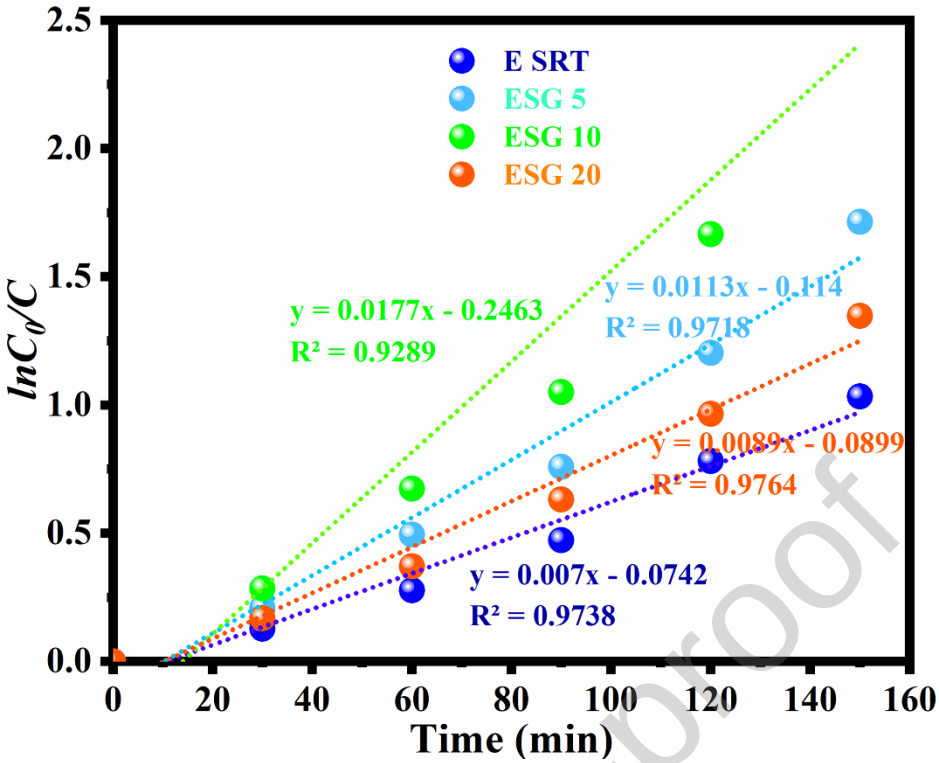

Fig. 10. First-order kinetic plot for the degradation of MB dye over E SRT, ESG 5, ESG 10 and ESG 20 photocatalysts

In the same way, the investigation of photocatalytic performance was assessed against the reduction of colourless 2-NP with the presence of ESG 10 photocatalyst under UV-Vis. light irradiation. The recorded UV-Vis. absorption spectra were demonstrated in Fig. 11 (a). From Fig. 11 (b), there is no reduction of 2-NP was occurred without the photocatalyst, with the presence of photocatalyst the peak observed at 280 nm concomitant peaks were diminished at different time intervals, hence the reduction was observed with 81 % of degradation efficiency. The above results revealed that ESG 10 photocatalyst can effectively degrade the 2-NP compound. Once again, the results confirm that the ESG 10 nanocomposite does not only degrade the coloured product but also degrades the organic molecules by similar photocatalytic reactions.

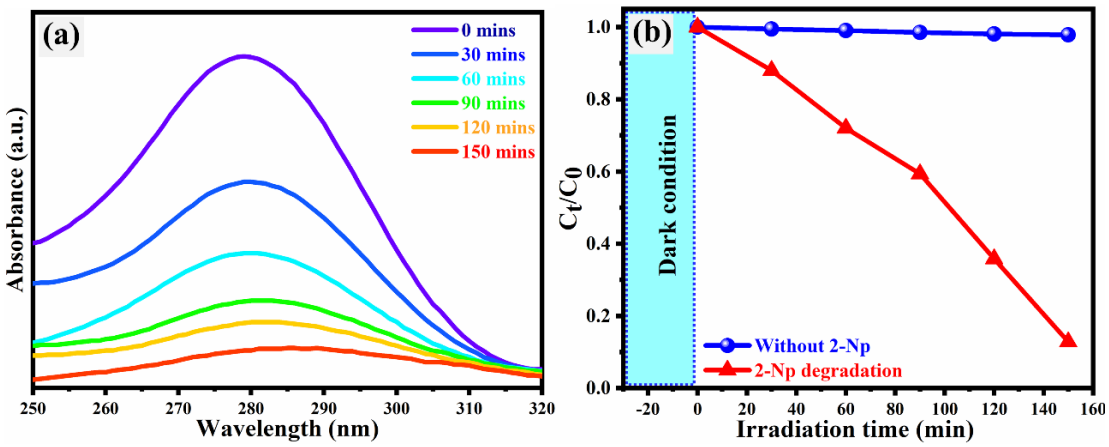

Fig. 11. (a) UV-Vis. absorption spectra and (b) photodegradation rate of 2-NP in the presence of ESG 10 photocatalyst

3.9 Scavenger test

The radicals involved in the photodegradation processes were determined by scavenger experiments with various scavenging agents. The various scavengers employed in this experiment are benzoquinone (1 mM) for superoxide radical ($O_2^{\bullet-}$), isopropyl alcohol (1mM) for hydroxyl alcohol ($OH^{\bullet}$) and ammonium oxalate for holes (h^+). As depicted in Fig. 12, without any scavengers ESG 10 photocatalyst shows no obvious changes in the degradation. By the addition of BQ, the degradation was drastically reduced from 91 % to 69.7 %, which indicates superoxide radical ($O_2^{\bullet-}$) played a role during the degradation process. With the addition of IPA ($OH^{\bullet}$) as a radical trapping agent, the degradation was suppressed to 48 % which reveals that hydroxide radical $OH^{\bullet}$ also played a role in the inhibition of e^-/h^+ pair recombination. Moreover, the photodegradation activity of ESG 10 was dramatically dropped more than other scavengers while the addition of AO for (h^+). The photodegradation process controlled by the species are in order as follows $O_2^{\bullet-} > OH^{\bullet} > h^+$. In the radical trapping experiments, O_2 is necessary for the separation of e^-/h^+ and the transfer of e^- from CB to O_2 solution is slower than from dyes to h^+. From these results, we may conclude that electron transport from the dye molecule to the holes dominates the photo-degradation of MB on 10 Wt. % of $SrTiO_3$-rGO (ESG 10) surface under ambient photocatalytic conditions.

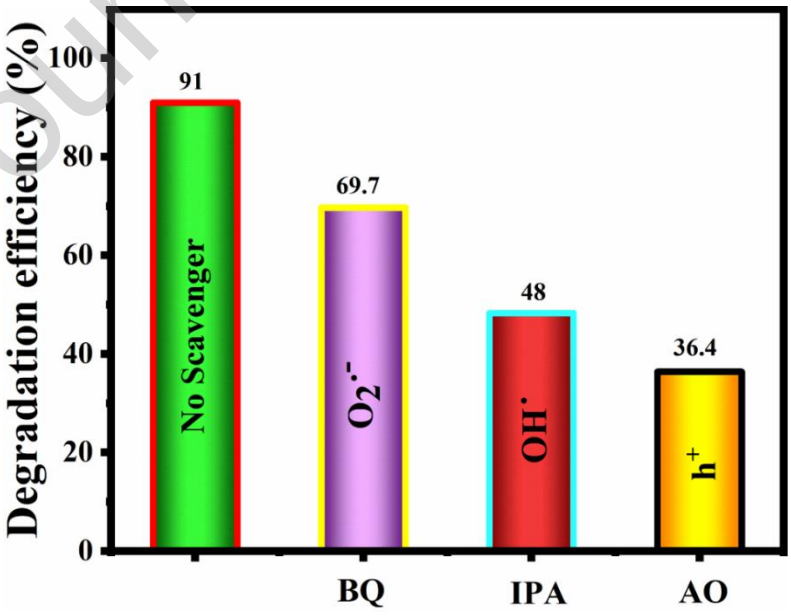

Fig. 12. Photodegradation of different scavengers over MB dye on ESG 10 photocatalyst

3.10 Recycle and stability test

The evaluation of stability for synthesized photocatalysts is investigated by recycling experiments. It is the most essential parameter to determine the sustainability of synthesized photocatalysts. In the typical experiment, ESG 10 photocatalyst was used for 4 consecutive runs over MB dye for 150 min under UV-Vis. light illumination. As shown in Fig. 13 (a), the degradation efficiency of the MB was drastically decreased after 4 consecutive runs of experiments. The loss in the degradation efficiency is due to catalyst loss during each cycle of the experiment. In addition, the XRD analysis was used to verify the crystallographic structure of the sample and the ESG 10 photocatalyst was not affected by any crystalline defects after the recycle experiment as shown in Fig. 13 (b). Therefore, the synthesised ESG 10 photocatalyst exhibits exemplary stability, efficient and non-photo corrosive material for practical photocatalytic applications. The degradation efficiency of the prepared ESG 10 photocatalyst, compared with earlier reported articles as shown in Table 1.

Table 1

Comparison study of dye degradation efficiencies by previously reported photocatalysts

S.No.	Photocatalyst	Degradation efficiency (%)	Reaction time (min)	Pollutant	References
1.	Polythiophene/$SrTiO_3$ nanocomposites	91	210	MB	[67]
2.	Cr/$SrTiO_3$ nanoparticles	60	180	MB	[68]
3.	Cu/$SrTiO_3$ nanoparticles	66	120	MB	[69]
4.	V doped $SrTiO_3$ nanocubes	83	120	MB	[70]
5.	Sulphur doped $SrTiO_3$	74.5	180	MB	[71]
6.	10 wt. % rGO/$SrTiO_3$ (ESG 10)	91 & 81	150	MB & 2-NP	This work

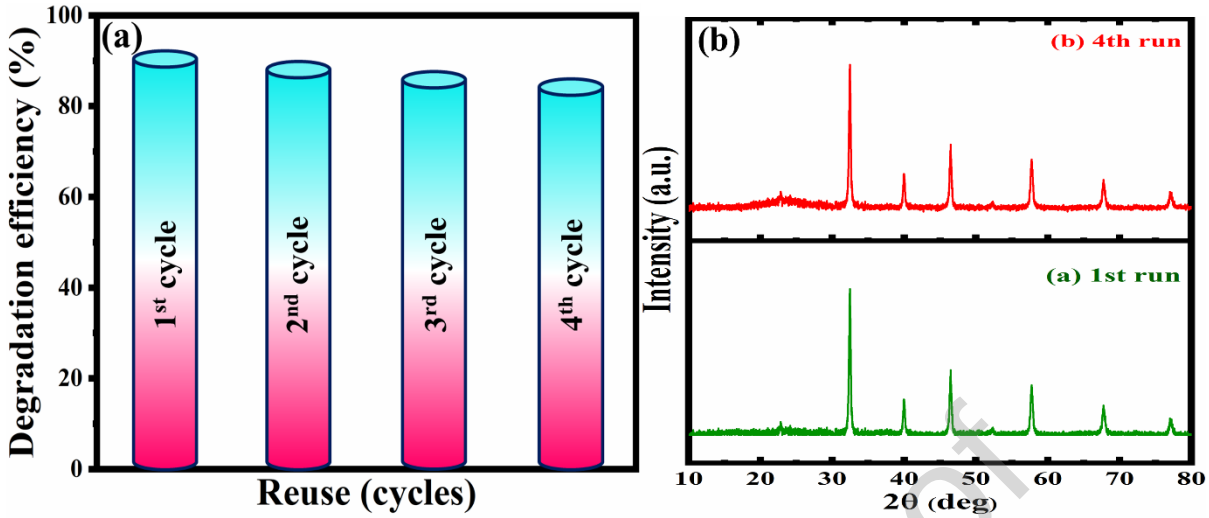

Fig. 13. (a) Degradation efficiency chart up to 4 cycles and (b) XRD pattern for 1st & 4th cycle of ESG 10 photocatalyst

3.11 Photocatalytic mechanism

To understand the plausible photocatalytic mechanism of rGO/$SrTiO_3$, the schematic representation was proposed in Fig. 14. The estimation of band edge position and its band edge potentials are essential parameters to affirm the photocatalytic degradation mechanism. The potentials of the conduction band (CB) and valence band (VB) plays a crucial role in the catalysis process are calculated by using the following empirical equation [72,73],

$$E_{VB} = \chi - E^c + 0.5E_g \quad (2)$$

$$E_{CB} = E_{VB} - E_g \quad (3)$$

Whereas E_{VB} is the VB edge potential, χ is the geometric means of electronegativity (5.34 eV) [40], E^c is the free electron energy on hydrogen's scale (4.5 eV) and E_g is the energy band gap of the semiconductor. From the above-mentioned equations, the CB and VB potential values are calculated and the obtained values are E_{CB} = -0.785 eV and E_{VB} = 2.465 eV respectively, for potential energy *versus* normal hydrogen electrode (NHE). The Fermi level of graphene is −0.008 V *vs* NHE [74]. The CB band potential is -0.785 eV, which is positive to the Fermi level of graphene. As a result, the intermediate energy level is below the CB of $SrTiO_3$ causes the photoexcited electrons could rapidly transfer from the CB of $SrTiO_3$ to rGO. The result shows that $SrTiO_3$ and rGO composite possess heterostructure formation, thereby the photoexcited e^-/h^+ pairs were suppressed and their separation efficiency was enhanced which could eventually enhance the photocatalytic degradation efficiency.

In the photocatalytic experiment process, when the illumination starts exposed on photocatalyst, both $SrTiO_3$ and rGO absorbs the light and are excited to generate

photoinduced e^-/h^+ pairs at CB and to VB. The generation of photoinduced e^- of $SrTiO_3$ and rGO transited from VB to CB and the h^+ were left behind at VB of $SrTiO_3$. Furtherly, the photoinduced e^- of $SrTiO_3$ facilitates the e^- transfer quickly to rGO, which is due to solid-solid intimately contacted interfaces. As a result, the introduction of rGO with its unique electronic structure enables facile charge separation and inhibits the charge recombination process. Furthermore, the enhanced light absorption and effective e^-/h^+ pair separation, transportation, and capture by the targeted molecules may occur due to synergistic effects [75]. During the photocatalytic process, the photogenerated e^- at CB is absorbed by O_2 molecules and reduced to $O_2^{\bullet-}$ by photoreduction process and the photogenerated h^+ at VB is directly decomposed from H_2O to $OH^\bullet$ radical by photooxidation process. Lastly, the $OH^\bullet$ and $O_2^{\bullet-}$ radicals ultimately respond with surface absorbed H_2O with a durable oxidizing agent through enhanced oxidation process over MB dye into CO_2, H_2O, mineral acids, etc., resultantly all these activities improve the photocatalytic degradation efficiency. The possible reaction mechanism is as follows;

$$SrTiO_3 + h\nu \rightarrow SrTiO_3 + (e^- + h^+) \quad (4)$$

$$SrTiO_3\,(e^-) + O_2 \rightarrow O_2^{\bullet-} \quad (5)$$

$$SrTiO_3\,(e^-) + rGO \rightarrow SrTiO_3 + rGO\,(e^-) \quad (6)$$

$$rGO\,(e^-) + O_2 \rightarrow O_2^{\bullet-} + rGO \quad (7)$$

$$SrTiO_3\,(h^+) + OH^- \rightarrow SrTiO_3 + OH^\bullet \quad (8)$$

$$OH^\bullet + MB \rightarrow H_2O + CO_2\ (Degraded\ Products) \quad (9)$$

$$O_2^{\bullet-} + MB \rightarrow H_2O + CO_2\ (Degraded\ Products) \quad (10)$$

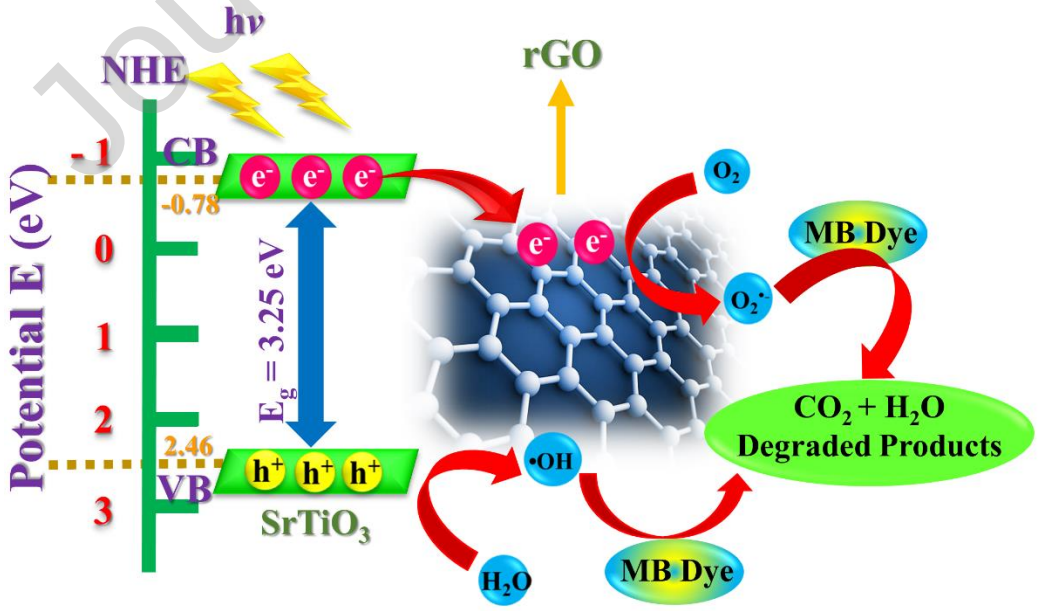

Fig. 14. Schematic representation of possible photocatalytic degradation mechanism

4. Conclusion

In summary, the rGO/$SrTiO_3$ agglomerated spherical shaped like morphological nanostructure with a Ti-C chemically bonded interface have been synthesized using rGO mediates with titanium hydroxide and strontium ions by facile hydrothermal method. The cubic phase structure and agglomerated spherical like morphology of $SrTiO_3$ perovskite were deduced by the XRD and FESEM studies. The formation of rGO/$SrTiO_3$ and its functional groups were investigated by FTIR analysis. The presence of various elements was confirmed by EDX analysis. The optical absorption spectra reveal positively shifted spectra by the incorporation of rGO. Thus, the study shows that the incorporation of rGO increases the charge separation efficiency which leads to enhance the photocatalytic activity. Among the synthesised photocatalysts ESG 10 exhibits with 91 % of MB dye degradation efficiency and 81 % of 2-NP reduction in 150 min under UV-Vis. irradiation. The stability of the photocatalyst was verified by the recycling experiment. Moreover, the synthesized ESG 10 nanocomposite has a profound ability on enhancing the photocatalytic property and it is affordable to design an efficient, recyclable and perovskite/graphene-based photocatalyst for environmental remediation application.

Declaration of Competing Interest

We don’t have any financial interest or personal relationships in this research work.

Acknowledgement

The authors are grateful to be the Researchers Supporting project number (RSP-2021/113), King Saud University, Riyadh, Saudi Arabia for the support.

References

[1] A. Kumar, S. Kumar, A. Bahuguna, A. Kumar, V. Sharma, V. Krishnan, Recyclable, bifunctional composites of perovskite type N-CaTiO 3 and reduced graphene oxide as an efficient adsorptive photocatalyst for environmental remediation, Mater. Chem. Front. 1 (2017) 2391–2404. https://doi.org/10.1039/C7QM00362E.

[2] C.-H. Shen, Y. Chen, X.-J. Xu, X.-Y. Li, X.-J. Wen, Z.-T. Liu, R. Xing, H. Guo, Z.-H. Fei, Efficient photocatalytic H2 evolution and Cr(VI) reduction under visible light using a novel Z-scheme SnIn4S8/CeO2 heterojunction photocatalysts, J. Hazard.

Mater. 416 (2021) 126217. https://doi.org/10.1016/j.jhazmat.2021.126217.

[3] J. Sun, C.-H. Shen, J. Guo, H. Guo, Y.-F. Yin, X.-J. Xu, Z.-H. Fei, Z.-T. Liu, X.-J. Wen, Highly efficient activation of peroxymonosulfate by Co3O4/Bi2WO6 p-n heterojunction composites for the degradation of ciprofloxacin under visible light irradiation, J. Colloid Interface Sci. 588 (2021) 19–30. https://doi.org/10.1016/j.jcis.2020.12.043.

[4] S. Kumar, A. Kumar, A. Kumar, V. Krishnan, Nanoscale zinc oxide based heterojunctions as visible light active photocatalysts for hydrogen energy and environmental remediation, Catal. Rev. 62 (2020) 346–405. https://doi.org/10.1080/01614940.2019.1684649.

[5] X.-J. Wen, Qian-Lu, X.-X. Lv, J. Sun, J. Guo, Z.-H. Fei, C.-G. Niu, Photocatalytic degradation of sulfamethazine using a direct Z-Scheme AgI/Bi4V2O11 photocatalyst: Mineralization activity, degradation pathways and promoted charge separation mechanism, J. Hazard. Mater. 385 (2020) 121508. https://doi.org/10.1016/j.jhazmat.2019.121508.

[6] M.R. Hoffmann, S.T. Martin, W. Choi, D.W. Bahnemann, Environmental Applications of Semiconductor Photocatalysis, Chem. Rev. 95 (1995) 69–96. https://doi.org/10.1021/cr00033a004.

[7] A. Kumar, A. Kumar, V. Krishnan, Perovskite Oxide Based Materials for Energy and Environment-Oriented Photocatalysis, ACS Catal. 10 (2020) 10253–10315. https://doi.org/10.1021/acscatal.0c02947.

[8] H. Zhang, X. Lv, Y. Li, Y. Wang, J. Li, P25-graphene composite as a high performance photocatalyst, ACS Nano. 4 (2010) 380–386. https://doi.org/10.1021/nn901221k.

[9] B. Jiang, C. Tian, Q. Pan, Z. Jiang, J.Q. Wang, W. Yan, H. Fu, Enhanced photocatalytic activity and electron transfer mechanisms of graphene/TiO2 with exposed {001} facets, J. Phys. Chem. C. 115 (2011) 23718–23725. https://doi.org/10.1021/jp207624x.

[10] O. Akhavan, Graphene nanomesh by ZnO nanorod photocatalysts, ACS Nano. 4 (2010) 4174–4180. https://doi.org/10.1021/nn1007429.

[11] T. Kavitha, A.I. Gopalan, K.P. Lee, S.Y. Park, Glucose sensing, photocatalytic and antibacterial properties of graphene-ZnO nanoparticle hybrids, Carbon N. Y. 50 (2012) 2994–3000. https://doi.org/10.1016/j.carbon.2012.02.082.

[12] G.L. He, Y.H. Zhong, M.J. Chen, X. Li, Y.P. Fang, Y.H. Xu, One-pot hydrothermal

synthesis of SrTiO3-reduced graphene oxide composites with enhanced photocatalytic activity for hydrogen production, J. Mol. Catal. A Chem. 423 (2016) 70–76. https://doi.org/10.1016/j.molcata.2016.05.025.

[13] Q. Xiang, J. Yu, M. Jaroniec, Preparation and enhanced visible-light photocatalytic H2- production activity of graphene/C3N4 composites, J. Phys. Chem. C. 115 (2011) 7355–7363. https://doi.org/10.1021/jp200953k.

[14] S. Yang, W. Li, C. Ye, G. Wang, H. Tian, C. Zhu, P. He, G. Ding, X. Xie, Y. Liu, Y. Lifshitz, S.-T. Lee, Z. Kang, M. Jiang, C 3 N-A 2D Crystalline, Hole-Free, Tunable-Narrow-Bandgap Semiconductor with Ferromagnetic Properties, Adv. Mater. 29 (2017) 1605625. https://doi.org/10.1002/adma.201605625.

[15] J. Low, J. Yu, W. Ho, Graphene-Based Photocatalysts for CO2 Reduction to Solar Fuel, J. Phys. Chem. Lett. 6 (2015) 4244–4251. https://doi.org/10.1021/acs.jpclett.5b01610.

[16] N. Zhang, Y. Zhang, Y.-J. Xu, Recent progress on graphene-based photocatalysts: current status and future perspectives, Nanoscale. 4 (2012) 5792. https://doi.org/10.1039/c2nr31480k.

[17] Z. Peng, S. Yang, D. Jia, P. Da, P. He, A.M. Al-Enizi, G. Ding, X. Xie, G. Zheng, Homologous metal-free electrocatalysts grown on three-dimensional carbon networks for overall water splitting in acidic and alkaline media, J. Mater. Chem. A. 4 (2016) 12878–12883. https://doi.org/10.1039/C6TA04426C.

[18] Y. Wang, C.-G. Niu, L. Wang, Y. Wang, X.-G. Zhang, G.-M. Zeng, Synthesis of fern-like Ag/AgCl/CaTiO 3 plasmonic photocatalysts and their enhanced visible-light photocatalytic properties, RSC Adv. 6 (2016) 47873–47882. https://doi.org/10.1039/C6RA06435C.

[19] A. Kumar, V. Navakoteswara Rao, A. Kumar, A. Mushtaq, L. Sharma, A. Halder, S.K. Pal, M.V. Shankar, V. Krishnan, Three-Dimensional Carbonaceous Aerogels Embedded with Rh-SrTiO 3 for Enhanced Hydrogen Evolution Triggered by Efficient Charge Transfer and Light Absorption, ACS Appl. Energy Mater. 3 (2020) 12134–12147. https://doi.org/10.1021/acsaem.0c02229.

[20] J. Liu, L. Zhang, N. Li, Q. Tian, J. Zhou, Y. Sun, Synthesis of MoS 2 /SrTiO 3 composite materials for enhanced photocatalytic activity under UV irradiation, J. Mater. Chem. A. 3 (2015) 706–712. https://doi.org/10.1039/C4TA04984E.

[21] L.F. Da Silva, W. Avansi, M.L. Moreira, A. Mesquita, L.J.Q. Maia, J. Andrés, E. Longo, V.R. Mastelaro, Relationship between crystal shape, photoluminescence, and

local structure in SrTiO 3 synthesized by microwave-assisted hydrothermal method, J. Nanomater. 2012 (2012) 1–6. https://doi.org/10.1155/2012/890397.

[22] Preparation of nanocrystalline strontium titanate (SrTiO 3) powder by sol-gel combustion method, Sci. Res. Essays. 8 (2013) 32–38. https://doi.org/10.5897/SRE12.592.

[23] K. Nakashima, M. Kera, I. Fujii, S. Wada, A new approach for the preparation of SrTiO3 nanocubes, Ceram. Int. 39 (2013) 3231–3234. https://doi.org/10.1016/j.ceramint.2012.10.009.

[24] S. Fuentes, R.A. Zarate, E. Chavez, P. Muñoz, D. Díaz-Droguett, P. Leyton, Preparation of SrTiO3 nanomaterial by a sol-gel-hydrothermal method, J. Mater. Sci. 45 (2010) 1448–1452. https://doi.org/10.1007/s10853-009-4099-y.

[25] S.F. Alvarado, F. La Mattina, J.G. Bednorz, Electroluminescence in SrTiO3:Cr single-crystal nonvolatile memory cells, Appl. Phys. A. 89 (2007) 85–89. https://doi.org/10.1007/s00339-007-4207-2.

[26] W. Dong, X. Li, J. Yu, W. Guo, B. Li, L. Tan, C. Li, J. Shi, G. Wang, Porous SrTiO3 spheres with enhanced photocatalytic performance, Mater. Lett. 67 (2012) 131–134. https://doi.org/10.1016/j.matlet.2011.09.045.

[27] Y.M. Rangel-Hernandez, J.C. Rendón-Angeles, Z. Matamoros-Veloza, M.I. Pech-Canul, S. Diaz-de la Torre, K. Yanagisawa, One-step synthesis of fine SrTiO3 particles using SrSO4 ore under alkaline hydrothermal conditions, Chem. Eng. J. 155 (2009) 483–492. https://doi.org/10.1016/j.cej.2009.07.024.

[28] S. Ouyang, H. Tong, N. Umezawa, J. Cao, P. Li, Y. Bi, Y. Zhang, J. Ye, Surface-Alkalinization-Induced Enhancement of Photocatalytic H 2 Evolution over SrTiO 3 -Based Photocatalysts, J. Am. Chem. Soc. 134 (2012) 1974–1977. https://doi.org/10.1021/ja210610h.

[29] Y. Jia, S. Shen, D. Wang, X. Wang, J. Shi, F. Zhang, H. Han, C. Li, Composite Sr2TiO4/SrTiO3(La,Cr) heterojunction based photocatalyst for hydrogen production under visible light irradiation, J. Mater. Chem. A. 1 (2013) 7905. https://doi.org/10.1039/c3ta11326d.

[30] P. Liu, J. Nisar, B. Pathak, R. Ahuja, Hybrid density functional study on SrTiO3 for visible light photocatalysis, Int. J. Hydrogen Energy. 37 (2012) 11611–11617. https://doi.org/10.1016/j.ijhydene.2012.05.038.

[31] F. Zou, Z. Jiang, X. Qin, Y. Zhao, L. Jiang, J. Zhi, T. Xiao, P.P. Edwards, Template-free synthesis of mesoporous N-doped SrTiO3 perovskite with high visible-light-

driven photocatalytic activity, Chem. Commun. 48 (2012) 8514–8516. https://doi.org/10.1039/c2cc33797e.

[32] D. Sui, X. Yin, H. Dong, S. Qin, J. Chen, W. Jiang, Photocatalytically Reducing CO2 to Methyl Formate in Methanol Over Ag Loaded SrTiO3 Nanocrystal Catalysts, Catal. Letters. 142 (2012) 1202–1210. https://doi.org/10.1007/s10562-012-0876-3.

[33] Y. Sun, J. Liu, Z. Li, Design of highly ordered Ag–SrTiO3 nanotube arrays for photocatalytic degradation of methyl orange, J. Solid State Chem. 184 (2011) 1924–1930. https://doi.org/10.1016/j.jssc.2011.05.037.

[34] S. Tonda, S. Kumar, O. Anjaneyulu, V. Shanker, Synthesis of Cr and La-codoped SrTiO 3 nanoparticles for enhanced photocatalytic performance under sunlight irradiation, Phys. Chem. Chem. Phys. 16 (2014) 23819–23828. https://doi.org/10.1039/C4CP02963A.

[35] A. Rosy, G. Kalpana, Reduced graphene oxide/strontium titanate heterostructured nanocomposite as sunlight driven photocatalyst for degradation of organic dye pollutants, Curr. Appl. Phys. 18 (2018) 1026–1033. https://doi.org/10.1016/j.cap.2018.05.019.

[36] M. Sethi, H. Bantawal, U.S. Shenoy, D.K. Bhat, Eco-friendly synthesis of porous graphene and its utilization as high performance supercapacitor electrode material, J. Alloys Compd. 799 (2019) 256–266. https://doi.org/10.1016/j.jallcom.2019.05.302.

[37] S. Kumar, V. Sharma, K. Bhattacharyya, V. Krishnan, N-doped ZnO–MoS 2 binary heterojunctions: the dual role of 2D MoS 2 in the enhancement of photostability and photocatalytic activity under visible light irradiation for tetracycline degradation, Mater. Chem. Front. 1 (2017) 1093–1106. https://doi.org/10.1039/C6QM00274A.

[38] M.J.S. Mohamed, U.S. Shenoy, D.K. Bhat, High Performance Dual Catalytic Activity of Novel Zinc Tungstate—Reduced Graphene Oxide Nanocomposites, Adv. Sci. Eng. Med. 9 (2017) 115–121. https://doi.org/10.1166/asem.2017.1977.

[39] A. Kumar, V. Navakoteswara Rao, A. Kumar, M. Venkatakrishnan Shankar, V. Krishnan, Interplay between Mesocrystals of CaTiO 3 and Edge Sulfur Atom Enriched MoS 2 on Reduced Graphene Oxide Nanosheets: Enhanced Photocatalytic Performance under Sunlight Irradiation, ChemPhotoChem. 4 (2020) 427–444. https://doi.org/10.1002/cptc.201900267.

[40] T. Xian, H. Yang, L. Di, J. Ma, H. Zhang, J. Dai, Photocatalytic reduction synthesis of SrTiO3-graphene nanocomposites and their enhanced photocatalytic activity, Nanoscale Res. Lett. 9 (2014) 327. https://doi.org/10.1186/1556-276X-9-327.

[41] C. He, X. Bu, S. Yang, P. He, G. Ding, X. Xie, Core-shell SrTiO3/graphene structure by chemical vapor deposition for enhanced photocatalytic performance, Appl. Surf. Sci. 436 (2018) 373–381. https://doi.org/10.1016/j.apsusc.2017.12.063.

[42] K. Ullah, L. Zhu, Z.-D. Meng, S. Ye, Q. Sun, W.-C. Oh, A facile and fast synthesis of novel composite Pt–graphene/TiO2 with enhanced photocatalytic activity under UV/Visible light, Chem. Eng. J. 231 (2013) 76–83. https://doi.org/10.1016/j.cej.2013.07.014.

[43] X. Mei, X. Meng, F. Wu, Hydrothermal method for the production of reduced graphene oxide, Phys. E Low-Dimensional Syst. Nanostructures. 68 (2015) 81–86. https://doi.org/10.1016/j.physe.2014.12.011.

[44] R. Abirami, C.R. Kalaiselvi, L. Kungumadevi, T.S. Senthil, M. Kang, Synthesis and characterization of ZnTiO3 and Ag doped ZnTiO3 perovskite nanoparticles and their enhanced photocatalytic and antibacterial activity, J. Solid State Chem. 281 (2020) 121019. https://doi.org/10.1016/j.jssc.2019.121019.

[45] G. Venkatesh, M. Geerthana, S. Prabhu, R. Ramesh, K.M. Prabu, Enhanced photocatalytic activity of reduced graphene oxide/SrSnO3 nanocomposite for aqueous organic pollutant degradation, Optik (Stuttg). 206 (2020) 164055. https://doi.org/10.1016/j.ijleo.2019.164055.

[46] G.-L. He, Y.-H. Zhong, M.-J. Chen, X. Li, Y.-P. Fang, Y.-H. Xu, One-pot hydrothermal synthesis of SrTiO3-reduced graphene oxide composites with enhanced photocatalytic activity for hydrogen production, J. Mol. Catal. A Chem. 423 (2016) 70–76. https://doi.org/10.1016/j.molcata.2016.05.025.

[47] M.A. Jalil, S.S. Chowdhury, M. Alam Sakib, S.M. Enamul Hoque Yousuf, E. Khan Ashik, S.H. Firoz, M.A. Basith, Temperature-dependent phase transition and comparative investigation on enhanced magnetic and optical properties between sillenite and perovskite bismuth ferrite-rGO nanocomposites, J. Appl. Phys. 122 (2017) 84902. https://doi.org/10.1063/1.4985840.

[48] M. Guo, Q. Liu, M. Wu, T. Lv, L. Jia, Novel reduced graphene oxide wrapped-SrTiO3 flower-like nanostructure with Ti–C bond for free noble metal decomposition of formic acid to hydrogen, Chem. Eng. J. 334 (2018) 1886–1896. https://doi.org/10.1016/j.cej.2017.11.120.

[49] J. Kong, Z. Rui, H. Ji, Enhanced Photocatalytic Mineralization of Gaseous Toluene over SrTiO 3 by Surface Hydroxylation, Ind. Eng. Chem. Res. 55 (2016) 11923–11930. https://doi.org/10.1021/acs.iecr.6b03270.

[50] M. Sharma, D. Mondal, A.K. Das, K. Prasad, Production of partially reduced graphene oxide nanosheets using a seaweed sap, RSC Adv. 4 (2014) 64583–64588. https://doi.org/10.1039/C4RA13149E.

[51] M. Varga, T. Izak, V. Vretenar, H. Kozak, J. Holovsky, A. Artemenko, M. Hulman, V. Skakalova, D.S. Lee, A. Kromka, Diamond/carbon nanotube composites: Raman, FTIR and XPS spectroscopic studies, Carbon N. Y. 111 (2017) 54–61. https://doi.org/10.1016/j.carbon.2016.09.064.

[52] S. Stankovich, R.D. Piner, S.B.T. Nguyen, R.S. Ruoff, Synthesis and exfoliation of isocyanate-treated graphene oxide nanoplatelets, Carbon N. Y. 44 (2006) 3342–3347. https://doi.org/10.1016/j.carbon.2006.06.004.

[53] H. Bantawal, U.S. Shenoy, D.K. Bhat, Tuning the Photocatalytic Activity of SrTiO 3 by Varying the Sr/Ti Ratio: Unusual Effect of Viscosity of the Synthesis Medium, J. Phys. Chem. C. 122 (2018) 20027–20033. https://doi.org/10.1021/acs.jpcc.8b06514.

[54] G. Li, Y. Ding, Y. Zhang, Z. Lu, H. Sun, R. Chen, Microwave synthesis of BiPO4 nanostructures and their morphology-dependent photocatalytic performances, J. Colloid Interface Sci. 363 (2011) 497–503. https://doi.org/10.1016/j.jcis.2011.07.090.

[55] Y. Bide, M.R. Nabid, B. Etemadi, Facile synthesis and catalytic application of selenium doped graphene/CoFe2O4 for highly efficient and noble metal free dehydrogenation of formic acid, Int. J. Hydrogen Energy. 41 (2016) 20147–20155. https://doi.org/10.1016/j.ijhydene.2016.08.108.

[56] U.S. Shenoy, H. Bantawal, D.K. Bhat, Band Engineering of SrTiO3: Effect of Synthetic Technique and Site Occupancy of Doped Rhodium, J. Phys. Chem. C. 122 (2018) 27567–27574. https://doi.org/10.1021/acs.jpcc.8b10083.

[57] B. Kiss, T.D. Manning, D. Hesp, C. Didier, A. Taylor, D.M. Pickup, A. V. Chadwick, H.E. Allison, V.R. Dhanak, J.B. Claridge, J.R. Darwent, M.J. Rosseinsky, Nano-structured rhodium doped SrTiO3–Visible light activated photocatalyst for water decontamination, Appl. Catal. B Environ. 206 (2017) 547–555. https://doi.org/10.1016/j.apcatb.2017.01.066.

[58] N. Yang, Y. Liu, H. Wen, Z. Tang, H. Zhao, Y. Li, D. Wang, Photocatalytic Properties of Graphdiyne and Graphene Modified TiO 2 : From Theory to Experiment, ACS Nano. 7 (2013) 1504–1512. https://doi.org/10.1021/nn305288z.

[59] X. Wu, S. Yin, Q. Dong, C. Guo, H. Li, T. Kimura, T. Sato, Synthesis of high visible light active carbon doped TiO2 photocatalyst by a facile calcination assisted solvothermal method, Appl. Catal. B Environ. 142–143 (2013) 450–457.

https://doi.org/10.1016/j.apcatb.2013.05.052.

[60] Z. Bo, X. Shuai, S. Mao, H. Yang, J. Qian, J. Chen, J. Yan, K. Cen, Green preparation of reduced graphene oxide for sensing and energy storage applications, Sci. Rep. 4 (2015) 4684. https://doi.org/10.1038/srep04684.

[61] H. Bantawal, M. Sethi, U.S. Shenoy, D.K. Bhat, Porous Graphene Wrapped SrTiO 3 Nanocomposite: Sr–C Bond as an Effective Coadjutant for High Performance Photocatalytic Degradation of Methylene Blue, ACS Appl. Nano Mater. 2 (2019) 6629–6636. https://doi.org/10.1021/acsanm.9b01513.

[62] M.M.J. Sadiq, U.S. Shenoy, D.K. Bhat, Synthesis of BaWO4/NRGO–g-C3N4 nanocomposites with excellent multifunctional catalytic performance via microwave approach, Front. Mater. Sci. 12 (2018) 247–263. https://doi.org/10.1007/s11706-018-0433-0.

[63] G. Zhu, T. Xu, T. Lv, L. Pan, Q. Zhao, Z. Sun, Graphene-incorporated nanocrystalline TiO2 films for CdS quantum dot-sensitized solar cells, J. Electroanal. Chem. 650 (2011) 248–251. https://doi.org/10.1016/j.jelechem.2010.10.011.

[64] N. Yang, J. Zhai, D. Wang, Y. Chen, L. Jiang, Two-dimensional graphene bridges enhanced photoinduced charge transport in dye-sensitized solar cells, ACS Nano. 4 (2010) 887–894. https://doi.org/10.1021/nn901660v.

[65] S.A. Ansari, M.M. Khan, M.O. Ansari, M.H. Cho, Silver nanoparticles and defect-induced visible light photocatalytic and photoelectrochemical performance of Ag@m-TiO2 nanocomposite, Sol. Energy Mater. Sol. Cells. 141 (2015) 162–170. https://doi.org/10.1016/j.solmat.2015.05.029.

[66] S.A. Ansari, M.M. Khan, M.O. Ansari, M.H. Cho, Gold nanoparticles-sensitized wide and narrow band gap TiO 2 for visible light applications: a comparative study, New J. Chem. 39 (2015) 4708–4715. https://doi.org/10.1039/C5NJ00556F.

[67] M. Faisal, F.A. Harraz, A.A. Ismail, A.M. El-Toni, S.A. Al-Sayari, A. Al-Hajry, M.S. Al-Assiri, Polythiophene/mesoporous SrTiO 3 nanocomposites with enhanced photocatalytic activity under visible light, Sep. Purif. Technol. 190 (2018) 33–44. https://doi.org/10.1016/j.seppur.2017.08.037.

[68] I.R. Qazi, W.-J. Lee, H.-C. Lee, M.S. Hassan, O.-B. Yang, Photocatalytic Degradation of Methylene Blue Dye Under Visible Light Over Cr Doped Strontium Titanate (SrTiO3) Nanoparticles, J. Nanosci. Nanotechnol. 10 (2010) 3430–3434. https://doi.org/10.1166/jnn.2010.2326.

[69] Q.I. Rahman, M. Ahmad, S.K. Misra, M. Lohani, Efficient Degradation of Methylene

Blue Dye Over Highly Reactive Cu Doped Strontium Titanate (SrTiO3) Nanoparticles Photocatalyst Under Visible Light, J. Nanosci. Nanotechnol. 12 (2012) 7181–7186. https://doi.org/10.1166/jnn.2012.6494.

[70] H. Bantawal, U.S. Shenoy, D.K. Bhat, Vanadium-Doped SrTiO3 Nanocubes: Insight into role of vanadium in improving the photocatalytic activity, Appl. Surf. Sci. 513 (2020) 145858. https://doi.org/10.1016/j.apsusc.2020.145858.

[71] K.H. Le, O.L.K. Pham, T.T. Tran, V.M. Le, Photocatalytic activities of sulfur doped SrTiO3 under simulated solar irradiation, Sci. Technol. Dev. J. 19 (2016) 176–184. https://doi.org/10.32508/stdj.v19i3.581.

[72] F. Dong, X. Xiao, G. Jiang, Y. Zhang, W. Cui, J. Ma, Surface oxygen-vacancy induced photocatalytic activity of La(OH) 3 nanorods prepared by a fast and scalable method, Phys. Chem. Chem. Phys. 17 (2015) 16058–16066. https://doi.org/10.1039/C5CP02460A.

[73] B.M. Pirzada, O. Mehraj, N.A. Mir, M.Z. Khan, S. Sabir, Efficient visible light photocatalytic activity and enhanced stability of BiOBr/Cd(OH) 2 heterostructures, New J. Chem. 39 (2015) 7153–7163. https://doi.org/10.1039/C5NJ00839E.

[74] C. Huang, C. Li, G. Shi, Graphene based catalysts, Energy Environ. Sci. 5 (2012) 8848. https://doi.org/10.1039/c2ee22238h.

[75] S.S. Patil, M.G. Mali, M.A. Hassan, D.R. Patil, S.S. Kolekar, S.-W. Ryu, One-Pot in Situ Hydrothermal Growth of BiVO4/Ag/rGO Hybrid Architectures for Solar Water Splitting and Environmental Remediation, Sci. Rep. 7 (2017) 8404. https://doi.org/10.1038/s41598-017-08912-z.

CRediT author statement

G. Venkatesh: Conceptualization; Supervision; Methodology; Writing - Review & editing; Project administration; Investigation; Writing - Original draft; Visualization;

S. Vignesh: Methodology; Data curation; Validation; Formal analysis;

M. Srinivasan: Supervision; Visualization; Resources; Formal analysis;

G. Palanisamy: Data curation; Validation; Formal analysis;

N. Elavarasan: Data curation; Validation; Formal analysis;

K. Bhuvaneswari: Data curation; Validation; Formal analysis;

P. Ramasamy: Data curation; Validation; Formal analysis;

Manawwer Alam: Data curation; Validation; Formal analysis;

Mohd Ubaidullah: Data curation; Validation; Resources; Formal analysis;

Md Kausar Rasa: Data curation; Validation; Resources; Formal analysis;

Declaration of interests

☒ The authors declare that they have no known competing financial interests or personal relationships that could have appeared to influence the work reported in this paper.

☐The authors declare the following financial interests/personal relationships which may be considered as potential competing interests:

Highlights

- The perovskite rGO/$SrTiO_3$ nanocomposite was prepared *via* facile hydrothermal route
- rGO possess interfacial contact with E SRT provides more charge transport ability
- ESG 10 photocatalyst achieves 91 % of MB dye degradation efficiency
- Possible degradation mechanism and charge transfer pathways were discussed
- The ESG 10 photocatalyst was utilized for 4 recycle runs with good stability

Graphical abstract